Mining, Metallurgy & Exploration
https://doi.org/10.1007/s42461-026-01605-0

Optical and Antibacterial Performance of Dy^{3+}/Tb^{3+} co-doped SnO_2 Nanoparticles Synthesized From the Green Synthesis of *Laurus nobilis L.* Extract

Mustafa Burak Coban[1,2] · Ozgen Omur Pekel[3] · Remziye Tulek[2] · Ali Teke[2] · Guler Yagiz Erdemir[4] · Orkun Babacan[5] · Fatma Unal[6,7] · Berna Koçer Kizilduman[8] · Mehmet Dogan[8]

Received: 10 April 2026 / Accepted: 19 May 2026
© The Author(s) 2026

Abstract
In the present study, an environmentally friendly method was used to synthesize Dy^{3+}, Tb^{3+}, Dy^{3+}/Tb^{3+} doped and undoped SnO_2 nanoparticles using *Laurus nobilis L.* extract as a reducing agent. The X-ray diffractograms confirmed that the detected planes correspond to the tetragonal-rutile phase and the absence of additional phases confirmed that it was obtained in a pure form. PL intensity decreased due to non-radiative transitions caused by increases in thermal energy and vibrational states as the temperature was raised from 10 K to room temperature. However, this decrease slowed down after 150 K. It is anticipated that these samples, as they approach a thermally stable state, may be considered potential candidates for optoelectronic applications. CIE diagrams of the nanostructures, for undoped SnO_2, the single-doped and co-doped samples shifted toward the white coordinate. Antibacterial tests conducted on synthesized nanoparticles showed that they exhibit good activity against both Gram-negative and Gram-positive bacteria.

Keywords Dy^{+3}/Tb^{+3} · SnO_2 · Co-precipitation method · Laurus nobilis L. · PL · Antibacterial efficiency

1 Introduction

Tin dioxide (SnO_2) is a wide band gap semiconductor (3.6–3.8 eV) distinguished by its excellent thermal stability, high optical transparency, and remarkable chemical durability. In addition, its mechanical robustness and ability to operate at relatively low temperatures further enhance its applicability. Owing to these properties, SnO_2 has been extensively employed in diverse fields, including photocatalysis, optoelectronic devices, solar cells, fluorescence-based sensors, and particularly gas-sensing technologies [1–7].

Beyond its well-established technological applications, nanosized SnO_2 has also garnered significant attention in the biomedical field due to its reported antibacterial efficacy against both *Gram-positive* and *Gram-negative* bacterial strains. The antimicrobial mechanism of SnO_2 nanoparticles is primarily attributed to the generation of reactive oxygen species (ROS) and the presence of oxygen vacancies, which collectively disrupt bacterial membranes and impair vital metabolic processes. Moreover, the development of SnO_2-based mixed ligand systems has been investigated to further enhance and broaden their antibacterial performance [8, 9].

✉ Mustafa Burak Coban
burakcoban@balikesir.edu.tr

1 Science and Technology Application and Research Center, Balikesir University, Balikesir, Türkiye
2 Department of Physics, Faculty of Science and Letter, Balikesir University, Balikesir, Türkiye
3 Department of Chemistry, Faculty of Science, Ankara University, Ankara, Türkiye
4 Department of Chemistry, Faculty of Science, Gazi University, Ankara, Türkiye
5 Department of Veterinary, Kepsut Vocational School, Balikesir University, Balikesir, Türkiye
6 Department of Biomedical Engineering, Faculty of Engineering and Natural Sciences, Samsun University, Samsun, Türkiye
7 Vocational School of Technical Sciences, Samsun University, Samsun, Türkiye
8 Department of Chemistry, Faculty of Science and Letter, Balikesir University, Balikesir, Türkiye

Published online: 28 May 2026

SnO_2 is also regarded as an ideal host matrix for the incorporation of trivalent rare earth ions (RE^{3+}), such as Sm^{3+}, Dy^{3+}, and Eu^{3+}. This preference arises from its natural abundance, outstanding thermal and chemical stability, and its capability to sustain high fluorescence efficiency, thereby rendering it highly suitable for the fabrication of nanocrystalline phosphor materials [10–13]. Among these dopants, Dy^{3+} ions exhibit two dominant emission bands: a yellow emission at ~575 nm ($^4F_{9/2} \rightarrow {}^6H_{13/2}$) and a blue emission at ~480 nm ($^4F_{9/2} \rightarrow {}^6H_{15/2}$) [13]. In contrast, Tb^{3+} ions are well known for their intense green emission centered at ~544 nm ($^5D_4 \rightarrow {}^7F_5$) [14]. Previous investigations have demonstrated that the co-doping of SnO_2 with Dy^{3+} and Tb^{3+} ions enables multi-color emission through the complementary spectral contributions of both dopants. This synergistic effect significantly enhances the optical performance of SnO_2-based nanophosphors, thereby broadening their potential applications in solid-state lighting and bioimaging technologies.

Parallel to these advances, increasing attention has been directed toward environmentally benign synthesis strategies for nanoparticles (NPs). Conventional chemical approaches—including hydrothermal, sol-gel, co-precipitation, electrospinning, spray pyrolysis, chemical vapor deposition, and combustion techniques—are often favored due to their relative simplicity, low cost, and mild reaction conditions [2, 4, 11, 13]. Nevertheless, these methods typically require high processing temperatures and involve toxic reagents, raising significant concerns regarding environmental sustainability [1]. To address these limitations, green synthesis methods have emerged as eco-friendly and facile alternatives. Plant-derived extracts from diverse biological sources, including leaves, fruit juices, seeds, stems, peels, barks, and roots, act simultaneously as natural reducing, capping, and stabilizing agents. Such biogenic strategies minimize reliance on hazardous chemicals, while aligning with the principles of the circular economy and directly contributing to the United Nations Sustainable Development Goals (SDGs) outlined in the 2030 Agenda [15–18].

Among the various plant-derived sources, *Laurus nobilis L.* holds particular significance. Owing to its richness in phenolic compounds, flavonoids, and essential oils, *Laurus nobilis* has been widely reported to exhibit potent antibacterial and antioxidant properties [19–22]. Extracts of *Laurus nobilis* have demonstrated inhibitory activity against several pathogenic microorganisms, including *Staphylococcus aureus*, *Escherichia coli*, *Enterococcus faecalis*, *Klebsiella pneumoniae*, and *Pseudomonas aeruginosa* [19, 21, 22]. Furthermore, previous studies have highlighted its ability to modulate oxidative stress and promote wound-healing processes, thereby reinforcing its biomedical significance [20]. The phytochemicals present in *Laurus nobilis* extract, particularly phenolic compounds and flavonoids, act as electron donors, facilitating the reduction of metal ions into nanoparticles. In addition, these biomolecules adsorb onto the nanoparticle surface, serving as capping and stabilizing agents that prevent aggregation and control particle growth.

Building on these considerations, the present study investigates the green synthesis of Dy^{3+} and Tb^{3+} co-doped SnO_2 nanoparticles using *Laurus nobilis L.* extract. This approach uniquely combines the luminescent benefits of RE^{3+} doping with the antimicrobial and eco-friendly attributes of plant-mediated synthesis. Dy^{3+} and Tb^{3+} ions are expected to generate strong and tunable photoluminescence across the visible spectrum, while the phytochemical-rich surface chemistry derived from *Laurus nobilis* contributes to enhanced antibacterial efficacy. To the best of our knowledge, this is among the first attempts to integrate rare-earth doping of SnO_2 with *Laurus nobilis*-assisted synthesis, resulting in a dual-functional nanomaterial with promising potential for applications in sustainable optoelectronics, bioimaging, and biomedical fields.

2 Experimental Details

2.1 Preparation of *Laurus nobilis L.* Extract

Laurus nobilis L. were freshly harvested from the mountains of Balikesir, Turkiye, and washed several times with distilled water to remove any contamination and remove dust, then dried in sunlight. Then, 50 g of dried leaves were heated in 500 mL of deionized water (DW) at 80 °C for 120 min. The acidic extraction solution (pH 5–6) was then filtered three times to remove any remaining residues or impurities. The obtained green synthesis extract was stored at +4 °C for the synthesis of the host and its dopants.

2.2 Green Synthesis of Undoped SnO_2 and (Dy^{3+}:Tb^{3+})-doped SnO_2 Nanoparticles Using *Laurus nobilis L.* Extract

NPs were synthesized by using the green synthesis-assisted co-precipitation method. For the synthesis of doping-free SnO_2 NPs, tin(IV) chloride pentahydrate was used as the raw material. A 0.1 M $SnCl_4 \cdot 5H_2O$ solution was mixed with an equal volume of 100 mL *Laurus nobilis L.* extract and heated at 80 °C for 2 h under magnetic stirring. The resulting mixture was then centrifuged for 10 min and washed three times with DW and EtOH. Finally, the synthesized SnO_2 NPs were dried in a drying oven at 100 °C overnight and calcined at 600 °C for 2 h, resulting in pure SnO_2 NP powder. Dy^{3+}, Tb^{3+}, and Dy^{3+} and Tb^{3+} co-doped SnO_2 NPs were synthesized using Dy(III) chloride hexahydrate and

Tb(III) chloride hexahydrate as raw materials.The synthesis of SnO_2 NPs doped with Dy^{3+} (5wt.%), Tb^{3+} (5wt.%), and Dy^{3+} (2.5 wt%):Tb^{3+} (2.5 wt%) was carried out using a systematic methodology similar to that employed for SnO_2 synthesis. Dy^{3+} and Tb^{3+} doping levels are expressed as molar substitution fractions (x) in $Sn_{1-x}Dy(Tb)_xO_2$, where Dy^{3+} and Tb^{3+} ions replace Sn^{4+} sites. For clarity, x = 2.5 and x = 5 correspond to 2.5 and 5 wt% relative to the total rare-earth cation content. This convention is used consistently throughout the manuscript. The raw materials Dy^{3+} and Tb^{3+} were prepared at the specified weight percentages, and tin(IV) chloride pentahydrate (0.1 M) was added to 100 mL of *Laurus nobilis L.* extract to form aliquots. The subsequent steps were carried out in systematic agreement with the synthesis of SnO_2 NPs based on the green synthesis-assisted precipitation methodology.

2.3 Characterization

XRD spectra of undoped SnO2 and doped Tb^{3+} and Dy^{3+} samples were obtained at 2θ scanning between 20° and 80° using Philips PW-1710/00 diffractometer with Cu-Kα radiation source (λ = 1.5418 Å). Thermogravimetric analysis of samples was performed using PerkinElmer Diamond simultaneous DT/TGA with a heating rate of 20 °C min^{-1} under a controlled nitrogen atmosphere in the temperature range from 30 °C to 600 °C. Surface morphology analyzes were performed using Zeiss EVO LS 10–55 Scanning Electron Microscope (SEM). The PL measurements were carried out on powders placed in closed-cycle cryostat in the temperature range of 10–300 K. In PL measurements, the samples were excited with a 349 nm frequency triple Nd: YLFQ switched pulse laser, dispersed with a 500 mm spectrometer using 1200 lines/mm grating, and detected with Intensified Charge Coupled Device (ICCD) camera.

2.4 Antibacterial Efficiency of the Sample

The antibacterial properties of the samples were evaluated against *Escherichia coli* and *Staphylococcus aureus* using the agar diffusion method, with bacterial strains obtained from the Culture Collection of the Department of Veterinary, Kepsut Vocational School, Balikesir University. Both bacteria were incubated in Nutrient Broth (Merck, Germany) at 37 °C for 24 h. After incubation, *E. coli* was cultured on MacConkey Agar (Merck, Germany) and *S. aureus* on Baird-Parker Agar, followed by incubation at 37 °C for 24 h.

After incubation, colonies were subjected to Gram staining, oxidase, catalase, and coagulase tests, growth in TSI agar, and assessment of colony characteristics on the agar media to confirm purity [23]. Pure cultures of *E. coli* and *S. aureus* were then adjusted to 0.5 McFarland turbidity standard. The turbidity was verified using a spectrophotometer at 620 nm wavelength.

The well diffusion method was used to measure the bacterial efficacy of the synthesized nanoparticles. In the Mueller-Hinton agar, wells were prepared by placing sterile 5 mm glass beads into the Petri dish using sterile forceps before pouring the agar. After the agar was poured, the glass beads were removed with sterile forceps, creating the wells. To evaluate the antibacterial properties of the samples, each bacterium was separately inoculated onto the surface of Mueller Hinton Agar (Merck, Germany) using a sterile swab. The samples were then placed separately in wells of the Mueller Hinton Agar and incubated at 37 °C for 24 h under aerobic conditions [24, 25].

The formation of a clear zone around the samples, indicating inhibition of bacterial growth, demonstrated the antibacterial activity of the samples. Samples that did not form an inhibition zone were considered to have no antibacterial effect against the tested bacteria [24].

The antibacterial activity of the synthesized samples was evaluated using the agar well diffusion method against Escherichia coli and Staphylococcus aureus. Following incubation, antibacterial efficacy was assessed by measuring the diameters of inhibition zones (mm) formed around each well. The diameters of inhibition zones were measured in millimeters using a calibrated ruler, including the diameter of the well. All measurements were recorded under identical experimental conditions for both bacterial species to enable direct comparison. As the assays were conducted as preliminary screening experiments, no statistical analysis (e.g., standard deviation or significance testing) was performed. Therefore, the results were interpreted using a descriptive and comparative approach based on inhibition zone diameters. This limitation should be carefully considered when interpreting the antibacterial performance of the tested formulations.

3 Results and Discussion

3.1 XRD Analysis

The X-ray diffraction (XRD) measurements of SnO_2 and Dy^{3+} (5wt.%), Tb^{3+} (5wt.%), as well as Dy^{3+}(2.5 wt%):Tb^{3+}(2.5wt.%) co-doped SnO_2 nanoparticles were carried out at room temperature over the 2θ range of 20–80°, employing a scanning rate of 2°/min. As illustrated in Fig. 1, the diffraction peaks are clearly observed at 26.41°, 33.75°, 37.81°, 51.74°, 54.56°, 57.73°, 61.74°, 64.64°, 65.87°, 71.26° and 78.76°, which can be assigned to the (110), (101), (200), (211), (220), (002), (310), (112), (301),

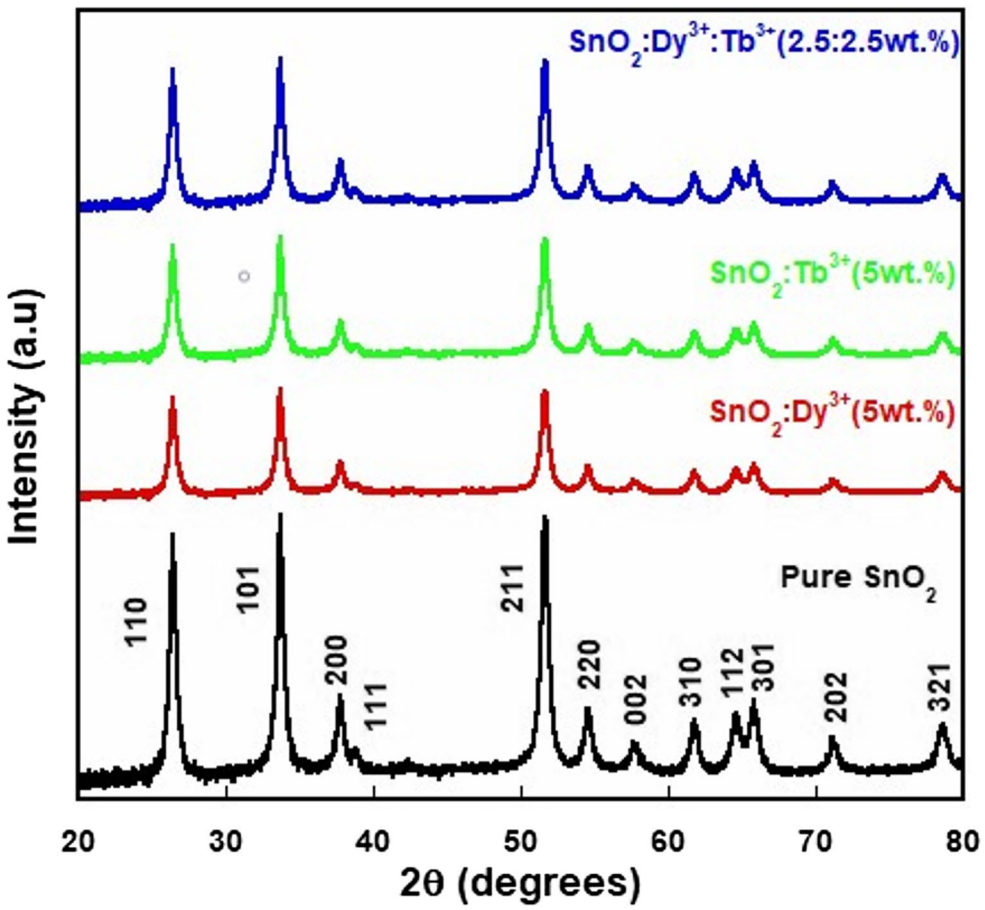


Fig. 1 XRD pattern for pure SnO_2, Tb^{3+}, Dy^{3+} and Dy^{3+}:Tb^{3+} doped SnO_2 nanoparticles

(202), and (321) lattice planes of the tetragonal rutile-type SnO_2 structure (JCPDS card no. 00–003-1114). The excellent agreement between the experimental reflections and the reference standard corroborates the successful formation of the rutile SnO_2 phase without the emergence of any impurity-related peaks, such as those of Dy_2O_3 or Tb_2O_3. The preservation of sharp and intense reflections further underscores the high crystallinity and structural integrity of the synthesized nanoparticles, thereby confirming that the rare-earth dopants were incorporated into the SnO_2 lattice without disrupting its long-range order. The crystallite size and lattice disorder of SnO_2 nanoparticles co-doped with Dy^{3+} and Tb^{3+} were systematically evaluated using the multi-line broadening approach (Debye–Scherrer), which allows for the reliable separation of size- and strain-induced contributions, similar to in-situ XRD peak profiling studies conducted on the nanoparticles. The average crystallite sizes and lattice distortions of the samples were determined as follows: for SnO_2 ($D = 28.288$ nm and $\delta = 1.249$ nm^{-2}), for SnO_2:Dy^{3+}(5 wt%) ($D = 32.805$ nm and $\delta = 0.929$ nm^{-2}), SnO_2:Tb^{3+}(5 wt%) ($D = 34.881$ nm and $\delta = 0.821$ nm^{-2}), and SnO_2:Dy^{3+}(2.5 wt%):Tb^{3+}(2.5 wt%) ($D = 33.089$ nm and $\delta = 0.913$ nm^{-2}), respectively. The average crystallite sizes indicate that doping promotes grain growth. Notably, doping further promotes grain growth; the Tb^{3+}-doped sample exhibits the largest average crystallite size, consistent with reduced lattice disorder.

3.2 Thermogravimetric Analysis

Thermogravimetric analysis serves as a method that elucidates the thermal stability characteristics of materials. Figure 2 indicates the thermogravimetric (TG) profiles of the examined samples. The weight reduction of the samples from which TG profiles are derived can be scrutinized in two distinct phases. The initial weight losses recorded within the temperature range of 30 °C to 80 °C are presumably attributable to the desorption of moisture present due to the conditions of growth and drying. The observed weight reductions occur at varying rates: 0.35% for pure SnO_2, 0.92% for SnO_2:Dy^{3+}(5wt%), 1.3% for SnO_2:Tb^{3+}(5%wt), and 1.1% for SnO_2:Dy^{3+}(2.5 wt%):Tb^{3+}(2.5 wt%). The initial rates of weight loss for the doped samples were significantly more rapid than those for pure SnO_2. It can be posited that dopant atoms, particularly terbium (Tb^{3+}), retain a greater quantity of moisture during the growth phase. A comparatively gradual decline in weight loss was recorded within the temperature spectrum of 80 °C to 600 °C for all

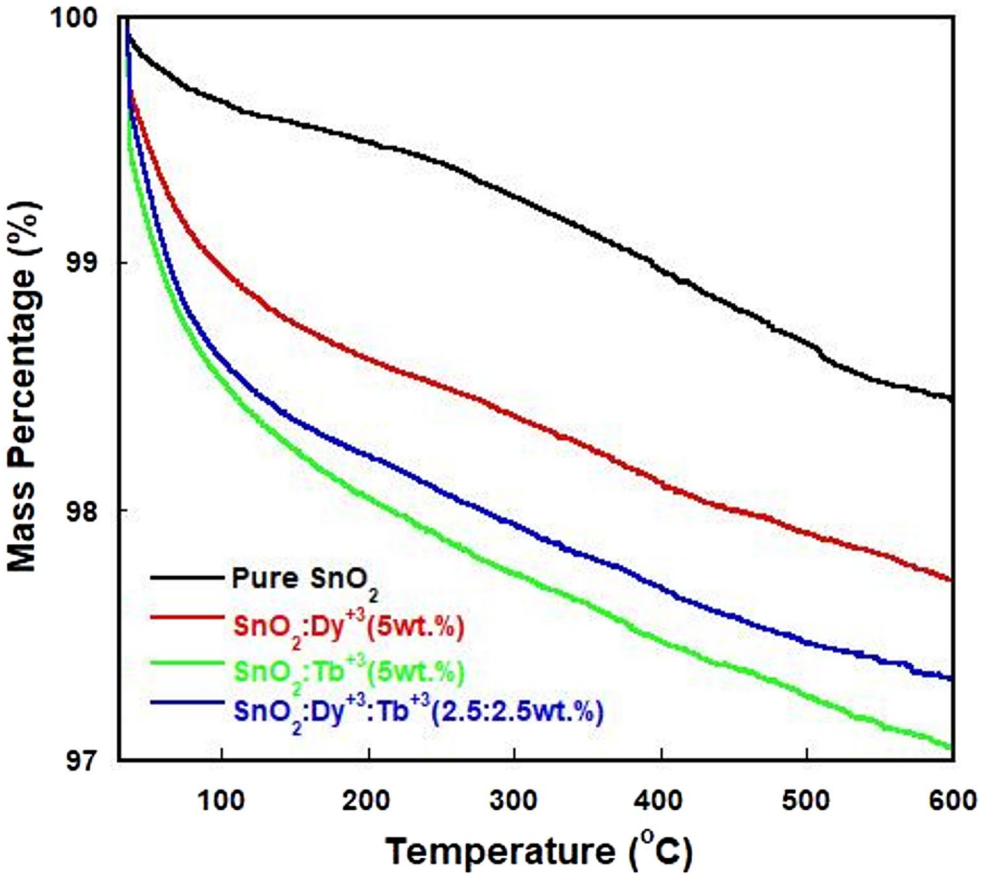


Fig. 2 TG curve of pure SnO_2, Tb^{3+}, Dy^{3+} and Dy^{3+}:Tb^{3+} doped SnO_2 NPs

samples. The percentage variations within this temperature range were computed to be approximately 1.2% for pure SnO_2, 1.4% for Dy^{3+}-doped samples, 1.7% for Tb-doped samples, and 1.6% for Dy^{3+}/Tb^{3+} co-doped samples, respectively. The slight weight loss observed above 100 °C can be associated with the removal of adsorbed and weakly bound water molecules present on the surface of the nanoparticles, as well as surface hydroxyl groups. The weight loss rate was noted to be comparatively elevated in the Tb^{3+}-doped samples, as evidenced by observations in the preceding temperature range. Nevertheless, given that the total weight loss recorded across all samples remains confined within the range of 1.5–3%, it can be asserted that all samples exhibit commendable structural and thermal stability.

3.3 SEM Analysis

The surface morphology of NPs was examined utilizing the scanning electron microscopy (SEM) technique. Figure 3 illustrates the SEM images alongside energy dispersive spectroscopy (EDS) analysis of the specimens. As evidenced by the SEM images, the surface morphology of pristine SnO_2 is predominantly characterized by irregularly shaped, agglomerated, and dispersed particles generally measuring less than one micron in size. Additionally, larger agglomerated particles are also observed in certain regions of the surface. Conversely, in the Dy^{3+} and Tb^{3+} ion-doped samples, there is a notable coalescence of smaller particles, resulting in smoother surfaces adorned with micron-sized particles. The particle dimensions appear significantly larger in the Tb^{3+}-doped samples compared to those in the Dy^{3+}-doped samples. The average diameter and size distribution of the nanoparticles were determined from SEM images using ImageJ software. Based on the ImageJ analysis, which averaged measurements from 100 individual particles, the average particle sizes of the nanoparticles were approximately 0.317 ± 0.306 µm for SnO_2, 0.444 ± 0.425 µm for SnO_2:Dy^{3+}(5 wt%), 0.624 ± 0.452 µm for SnO_2:Tb^{3+}(5 wt%), and for SnO_2:Dy^{3+}(2.5 wt%):Tb^{3+}(2.5 wt%) 0.561 ± 0.444, respectively. In the Dy^{3+}/Tb^{3+} co-doped sample, the degree of agglomeration increased once more, causing the surface morphology to begin resembling that of pure SnO_2.

EDS was employed to ascertain the elemental composition of the synthesized samples. The values representing both weight and atomic percentages for each element are depicted in Fig. 3. These observed percentage values are approximately congruent with the intended values. The spectral peaks corresponding to Sn, O, Dy, and Tb elements identified in the EDS spectra furnish compelling evidence

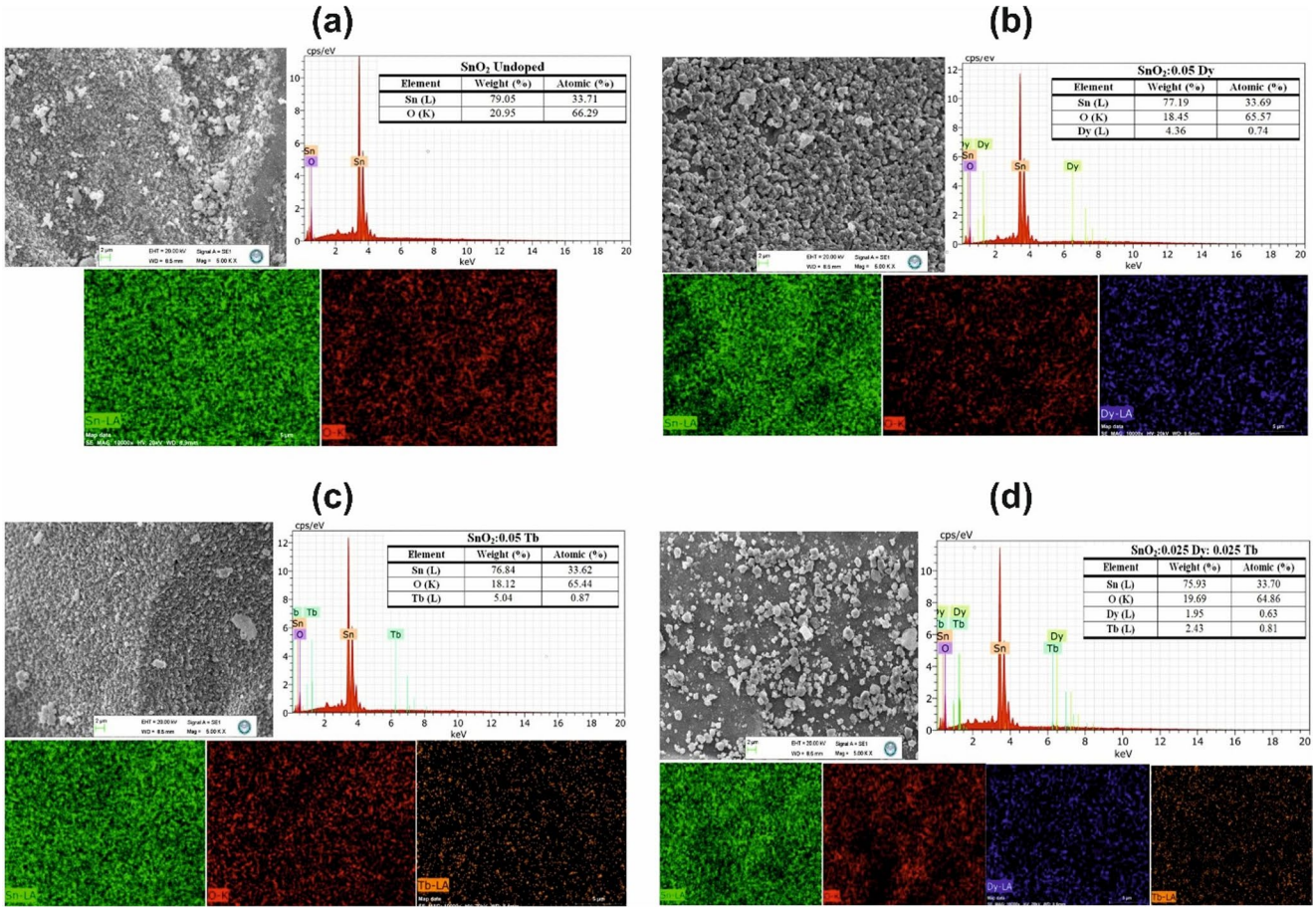


Fig. 3 The SEM images with EDS and Elemental mapping of (**a**) pure SnO_2, (**b**) SnO_2:Tb^{3+}, (**c**) SnO_2:Dy^{3+} and (**d**) SnO_2:Dy^{3+}:Tb^{3+} nanoparticles

regarding their compositional presence within the matrix. The EDS spectra obtained corroborate the findings from XRD analysis, indicating the successful incorporation of Dy^{3+} and Tb^{3+} ions into the SnO_2 matrix. Furthermore, elemental mapping reveals that the doping process is executed uniformly across the surface.

3.4 PL Analysis

RE^{3+} luminescent materials are widely used in many fields and have become one of the most important areas of RE applications. Therefore, the PL characteristics of RE^{3+} luminescent materials contain important information for many applications [26]. To analyze the mechanism of Dy^{3+} ion doping on the luminescence intensity of the samples in more detail, the emission spectra were tested at a wavelength of 349 nm under Dy^{3+}, Tb^{3+}, and Dy^{3+}/Tb^{3+} ion characteristic excitation. Figure 4a and b show the room temperature emission spectrum of the Dy^{3+}, Tb^{3+}, and Dy^{3+}/Tb^{3+} doped SnO_2 structure and the energy level diagrams of the possible radiative transitions of Dy^{3+} and Tb^{3+} RE ions, respectively. In Fig. 4a, two emission peaks belonging to Dy^{3+} were detected when the Dy^{3+} doped sample was excited, namely $^4F_{9/2}\rightarrow{}^6H_{15/2}$ (480 nm) and $^4F_{9/2}\rightarrow{}^6H_{13/2}$ (574 nm). These characteristic PL bands are in agreement with those observed in some Dy^{3+} and Tb^{3+} doped luminescent materials found in the literature [27–30]. When the Tb^{3+} doped sample was excited, four emission peaks belonging to Tb^{3+} were detected, namely $^5F_4\rightarrow{}^7F_6$ (492 nm), $^5F_4\rightarrow{}^7F_5$ (543 nm), $^5F_4\rightarrow{}^7F_4$ (583 nm), and $^5F_4\rightarrow{}^7F_3$ (619 nm) [31]. However, there was a Tb^{3+} emission peak with high peak intensity, indicating an energy transfer process between Dy^{3+} and Tb^{3+} ions. Due to cross-relaxation between Tb^{3+} and Dy^{3+} ions, when Tb^{3+} and Dy^{3+} are co-doped into the structure, radiation energy transfer cannot occur at the excitation wavelength, indicating that Tb^{3+} ions are sensitized by Dy^{3+} ions. The emission intensity of Dy^{3+} (as the sensitizer) decreased when it transitioned from the excited state to a lower level. The energy was transferred to Tb^{3+} for the $^5D_4\rightarrow{}^7F_J$ level transition, which significantly improved the green emission of $^5D_4\rightarrow{}^7F_5$ [32].

Low-temperature luminescence highlights radiative processes that compete with non-radiative decay activated by temperature; this emphasizes quantum-coherent spectral

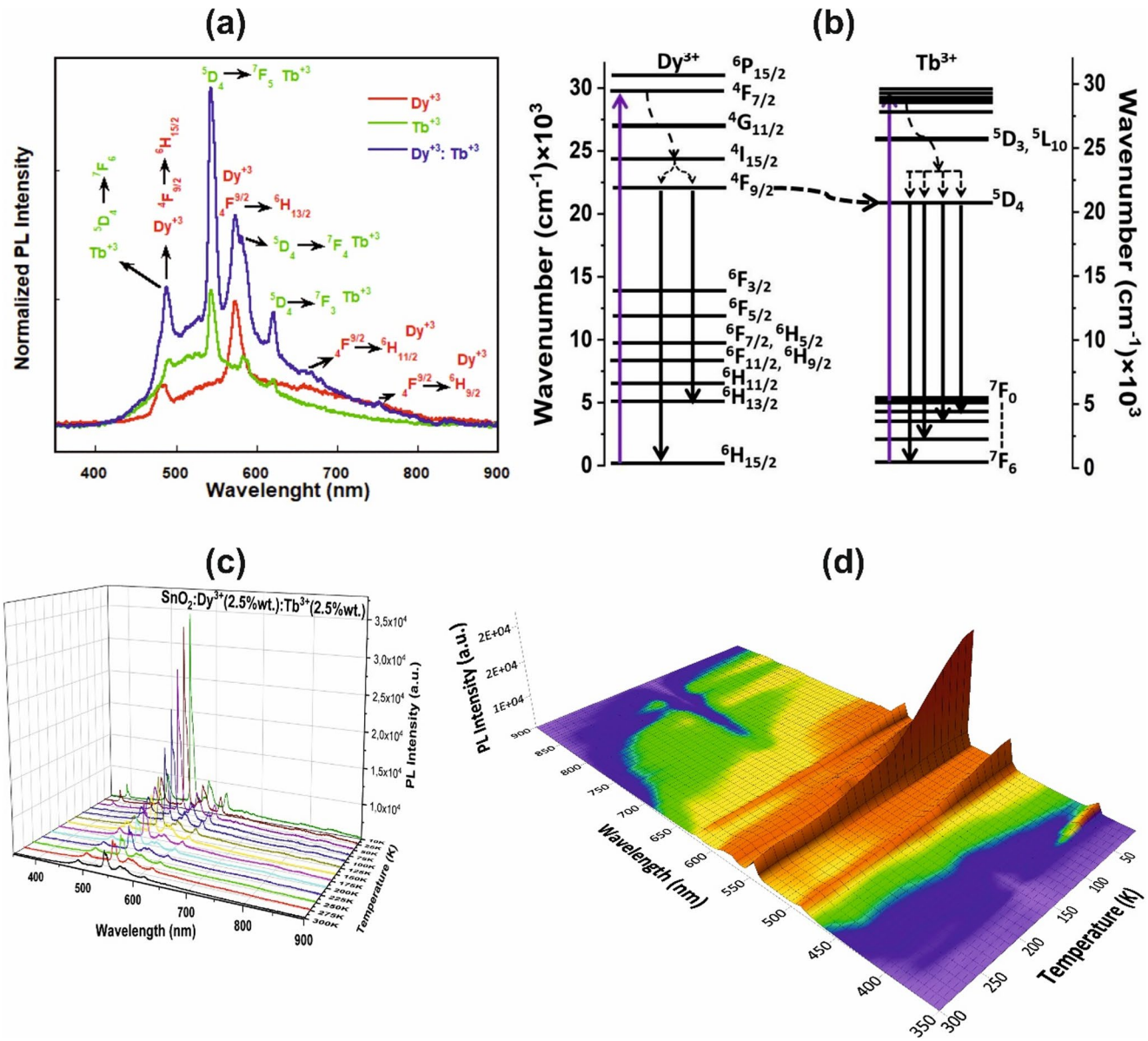


Fig. 4 (**a**) PL emission spectra of SnO_2 doped with terbium (Tb^{3+}), dysprosium (Dy^{3+}), and co-doped with both Dy3 + and Tb3 + nanoparticles at ambient temperature, (**b**) Diagrammatic representation of the energy level structure and energy transitions of Dy^{3+} and Tb^{3+}. (**c**) 3D PL emission spectra of SnO_2:Dy^{3+}:Tb^{3+} with temperature increments of 25 K across the range of 10–300 K, (**d**) Isometric graph of photoluminescence (PL) intensity as a function of wavelength and temperature for SnO_2:Dy^{3+}:Tb^{3+} in the temperature range of 10 to 300 K

features that emerge when fluorescence (fast singlet decay), phosphorescence (inter-system transitions to long-lived triplets), and phonon coupling decrease. Understanding these mechanisms explains why low temperatures give rise to weak emission states and prolong the lifetime of triplet-mediated emission. Low temperature alters both spectral shapes and kinetics by reducing phonon coupling, slowing thermally activated quenching, and modifying carrier trap dynamics via energy transfer; these changes are directly observable in steady-state spectra and time-resolved decay measurements. Examples in organic and inorganic systems show that when cooled to cryogenic temperatures, phosphorescence lifetimes increase, new emissions emerge, and mode separation occurs. Low-temperature luminescence forms the basis for analytical thermometry, material characterization, biosensor prototypes, and optoelectronic research; recent trends promote ultra-long organic phosphorescence supported by advanced analysis, limited metal cluster engineering, and multi-parameter luminescence thermometry [33, 34]. For an in-depth examination of the influence of temperature on the luminescence mechanism, the temperature-dependent photoluminescence (PL) spectrum and isometric plot for the SnO_2:(2.5wt%) Dy^{3+}:(2.5wt%)Tb^{3+} NPs within the temperature spectrum of 10 to 300 K are illustrated in Fig. 4c and d. Initially, it is

imperative to highlight that the distributions and morphologies of the peak positions are analogous across the samples. Moreover, no novel spectral emission bands or pronounced splitting were observed. It is well-established that substantial line broadening, diminished transition intensities, and the occurrence of unresolved peaks at elevated temperatures complicate the characterization of luminescence. Examination of Fig. 4c and d reveals notable intensity variances between the temperatures of 300 K and 10 K. As hypothesized, the gradual elevation of temperature corresponds to a progressive decline in PL intensity, attributable to thermal quenching (TQ) and non-radiative losses [35, 36]. We propose that the analysis of thermal quenching mechanisms is predicated on the following rationale. As temperature ascends, the interaction of photons intensifies, and free electrons residing in the lowest excited state transition back to the ground state through non-radiative processes at the juncture where the excited and ground states converge, thus resulting in energy dissipation from the photon energy. Further elevation of temperature engenders an increase in thermal energy. Correspondingly, with the augmentation of thermal energy, a greater frequency of non-radiative transitions is observed, culminating in a marked reduction in emission intensity [37]. As depicted in Fig. 4c, the transition of temperature from 10 K to 150 K induced a dramatic reduction in PL intensity due to thermal quenching. Conversely, when the temperature was incrementally raised beyond 150 K, the rate of decrease became considerably attenuated. This observation suggests that luminescent materials may achieve thermal stability at high temperatures, making them an intriguing candidate for optoelectronic devices applicability.

CIE color coordinates and correlated color temperature (CCT) values are important parameters for determining the performance of industrial products/equipment and solid-state lighting systems. Lighting characteristics comply with the 1931 CIE color coordinates, and the color of any light source can be marked and represented at its (x, y) coordinates in this color space; this can be used to measure and represent the light color level of luminous materials [38, 39]. In general, color temperature (CCT) can be obtained from the following formula data [40].

$$CCT = -437n^3 + 3601n^2 - 6861n + 5524.31$$

$$n = \frac{x - 0.3320}{y - 0.1858}$$

where n represents the parameter, and x and y represent the chroma coordinates. CCT values were calculated at excitation wavelengths with different dopant types and concentrations.

Following the PL spectra presented in Fig. 4a and c, and 4d, the luminescent materials excited at 349 nm were evaluated, and the corresponding two-dimensional CIE diagram is shown in Fig. 5a and b. The CIE (x, y) values calculated based on room temperature and temperature are listed in Tables 1 and 2. Compared to undoped SnO_2, the (x) and (y) color coordinates of the Dy^{3+}, Tb^{3+}, and Dy^{3+}/Tb^{3+} nano-phosphors at the 349 nm excitation wavelength are (0.311, 0.316), (0.308, 0.319), and (0.312, 0.329), representing neutral white light emission. Furthermore, low-temperature measurements cause a noticeable change in the CIE coordinates. Temperature-dependent CIE coordinates were determined for the equally doped sample. Due to the significant ET between Tb3 + and Dy3+, the emission color of the equally doped nano-phosphor (2.5%wt Dy^{3+}/2.5%wt Tb^{3+}) shifts from the white spectral region (0.312,0.329) at room temperature to the yellowish-green spectral region (0.310, 0.368) as the temperature decreases towards 10 K. In phosphor structures doped with both Tb^{3+} and Dy^{3+}, the overall emission colors can be shifted from warm white to the yellowish-green spectral region, offering more application options [41].

3.5 Antibacterial Efficiency of Structures

Metal and metal oxide nanoparticles derived from plant extracts exhibit excellent stability over extended periods [42]. All tested SnO_2-based samples incorporating *Laurus nobilis* extract exhibited measurable antibacterial activity against both *Escherichia coli* and *Staphylococcus aureus*, as indicated by the formation of inhibition zones. A comparative evaluation of inhibition zone diameters revealed distinct response patterns between the two bacterial species. Against *E. coli*, inhibition zones varied between 6 and 10 mm, indicating differential antibacterial performance among the tested samples. The SnO_2:2.5 Dy^{3+}:2.5 Tb^{3+} formulation exhibited the largest inhibition zone (10 mm), while undoped SnO_2 showed the lowest activity (6 mm), and the remaining doped samples demonstrated intermediate effects (8 mm). These findings suggest a modest variation in antibacterial activity depending on nanoparticle composition. In contrast, all samples produced identical inhibition zone diameters (10 mm) against *S. aureus*, indicating a uniform antibacterial response irrespective of compositional differences. This lack of variation suggests that, under the applied experimental conditions, nanoparticle modification did not result in a measurable differentiation in activity against this organism.

When both bacterial species are directly compared, *S. aureus* appears to exhibit relatively higher susceptibility under the tested conditions, as reflected by uniform and relatively larger inhibition zones compared to the more variable

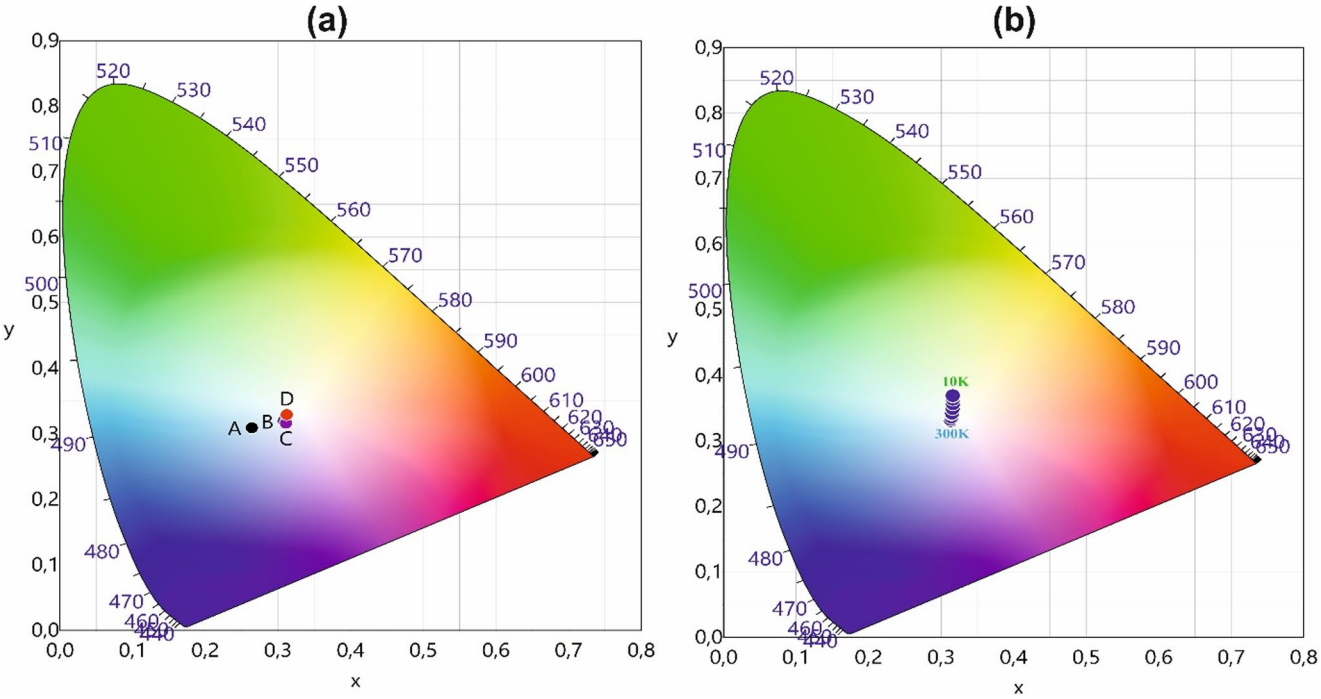


Fig. 5 (**a**) CIE coordinate diagram of all samples at room temperature, (**b**) Temperature dependent CIE coordinate diagram of SnO_2:Dy^{3+}(2.5%wt.): Tb^{3+}(2.5%wt.)

Table 1 The CIE coordinates and CCT values of pure SnO_2, SnO_2:Tb^{3+}(5%wt.), SnO_2:Dy^{3+}(5%wt.) and SnO_2:Dy^{3+}(2.5%wt.):Tb^{3+}(2.5%wt.) luminecent materials at room temperature

Sample	CIE chromaticity coordinates (x, y)		CCT value (K)
SnO_2	0.264	0.309	6164
SnO_2:Tb^{3+}(5wt.%)	0.308	0.319	6718
SnO_2:Dy^{3+}(5 wt%)	0.311	0.316	6869
SnO_2:Dy^{3+}(2.5 wt%): Tb^{3+}(2.5 wt%)	0.312	0.329	6542

Table 2 The CIE coordinates and CCT values of SnO_2:Dy^{3+}(2.5wt.%): Tb^{3+}(2.5wt.%) nanoparticles from 300 K to 10 K

Temperature (K)	CIE chromaticity coordinates (x, y)		CCT value (K)
300	0.312	0.329	6542
275	0.312	0.330	6490
250	0.312	0.329	6498
225	0.313	0.330	6472
200	0.313	0.332	6461
175	0.314	0.336	6385
150	0.314	0.340	6347
125	0.315	0.342	6300
100	0.315	0.348	6228
75	0.316	0.356	6177
50	0.316	0.363	6147
25	0.316	0.368	6134
10	0.31	0.368	6134

and, in some cases, smaller zones observed for *E. coli*. This difference may be attributed to fundamental structural distinctions between Gram-positive and Gram-negative bacteria, particularly the presence of an outer membrane in *E. coli*, which can act as a permeability barrier to antimicrobial agents. Therefore, the present findings should be considered preliminary and primarily indicative of comparative antibacterial tendencies under the tested conditions.

It should be noted that the observed differences in inhibition zone diameters are relatively limited in magnitude. Furthermore, as the measurements were obtained from preliminary screening experiments, the results should be interpreted as indicative of general trends rather than statistically validated differences. Additional studies incorporating replicate experiments and quantitative statistical analysis would be required to confirm and further substantiate these observations. Also all compounds has the same zone diameter against *S. aureus*. The inhibition zone diameters produced by SnO_2 and Laurus nobilis L. extract compounds against both bacterial strains are summarized in Table 3, while representative images of the zones are illustrated in Fig. 6.

The antibacterial activity of SnO_2 NPs can be explained by several mechanisms as follows. The antimicrobial activity of SnO_2 NPs is attributed to the presence of superoxide and hydroxyl radicals, which lead to the formation of H_2O_2. The hydrogen peroxide penetrates the cell, disrupting the composition of the cytoplasm, ultimately inhibiting

Table 3 Zone diameters of SnO_2 and Laurus nobilis L. extract compounds against *E. coli* and *S. aureus*

SnO and Laurus nobilis L. extract compounds	Codes of SnO and Laurus nobilis L. extract compounds in study	Zone diameters against E. coli (mm)	Zone diameters against S. aureus (mm)
SnO_2	A	6	10
SnO_2:5wt.%Dy^{3+}	B	8	10
SnO_2:5wt.%Tb^{3+}	C	8	10
SnO_2:2.5wt.%Dy^{3+}:2.5wt.Tb^{3+}	D	10	10

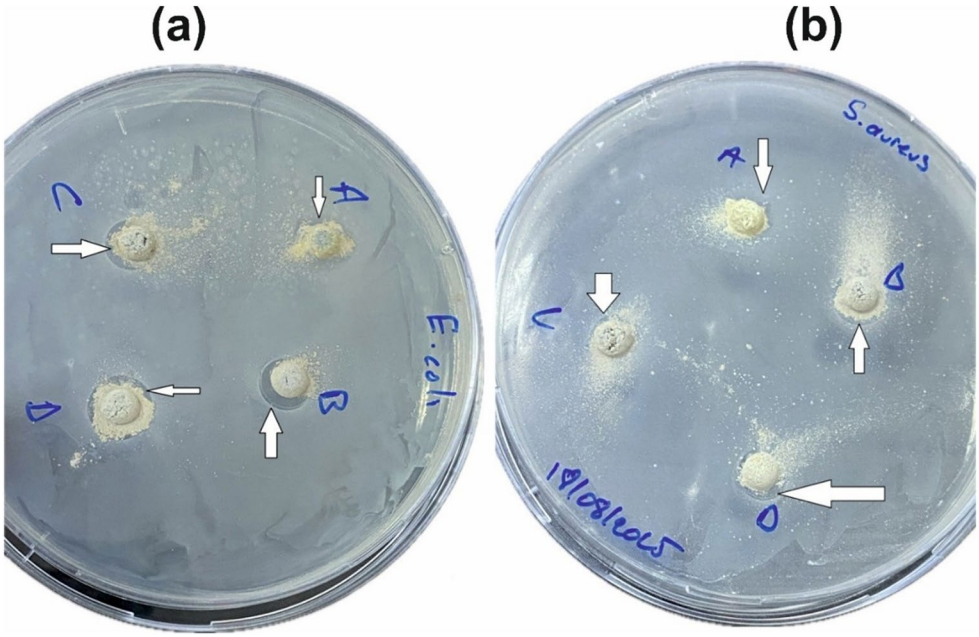


Fig. 6 (**A**) SnO_2, (**B**) SnO_2:5wt%Dy^{3+}, (**C**) SnO_2:5wt%Tb^{3+}, and (**D**) SnO2:2.5wt%Dy^{3+}:2.5wtTb^{3+} nanoparticles showing inhibition zones against *E. Coli (left)* and *S. Aureus* (right) with antibacterial activity

the survival of the microorganism [43, 44]. Another proposed mechanism involves SnO_2 NPs inducing damage to bacterial cell membranes, thereby increasing membrane permeability and facilitating the leakage of intracellular constituents. This disruption can result in structural membrane damage and the formation of pores, ultimately compromising cellular integrity and leading to bacterial cell death [44]. Compared to the zone diameters reported by Gopal et al. [45] against *E. coli* and *S. aureus*, the results of this study were found to be similar for *E. coli*, but showed a larger zone diameter against *S. aureus* than that reported by Gopal et al. [45]. In the study conducted by Muhammed et al. [44], it was reported that the material was most effective against *E. coli*. In contrast, the findings of the present study, based on the measured zone diameters, indicate greater effectiveness against *S. aureus*. The antibacterial activity of the SnO_2 molecule against *Staphylococcus aureus* and *Escherichia coli*, as reported by Pandimurugan and Sankaranarayanan [46], aligns with the findings observed in the present study. According to the zone diameters against *E. coli* and *S. aureus* reported in the study by Haq et al. [43], this study demonstrated larger zones of inhibition in millimeters for both bacteria. John et al. [47] reported the antibacterial activity of SnO_2 nanoparticles against *E. coli* and *S. aureus* by measuring inhibition zone diameters. When compared to their study, similar results were observed for *E. coli*, whereas in the present study, a stronger antibacterial effect was noted against *S. aureus*.

Laurus nobilis is known to possess antimicrobial, cytotoxic, and immunomodulatory properties. Its essential oil contains compounds such as eucalyptol, α-terpinyl acetate, linalool, methyl eugenol, sabinene, and carvacrol. The composition and properties of the essential oil can vary depending on factors such as the country of harvest, altitude, duration of sunlight exposure, and harvesting conditions. These essential oil components of *L. nobilis* exhibit strong antibacterial activity against both Gram-negative and Gram-positive foodborne pathogens (such as *Salmonella*, *Staphylococcus aureus*, *Escherichia coli*, and *Listeria monocytogenes*), as well as spoilage bacteria (*Pseudomonas aeruginosa*) and also demonstrate antifungal effects [48].

One of the important properties of essential oils and their components is their hydrophobicity, which enables them to interact with the lipid components of bacterial cell membranes and mitochondria. This interaction disrupts the cell structures, increasing their permeability. The antimicrobial activity of essential oils depends not only on their chemical composition but also on their lipophilic properties, the

strength of functional groups, and their aqueous solubility. A mixture of compounds with different biochemical properties can enhance the overall effectiveness of essential oils [48].

Phytochemicals are employed for the reduction and stabilization of nanoparticles. These phytochemicals may enhance the antibacterial activity of the nanoparticles by initiating or accelerating a series of events, including the generation of reactive oxygen species (ROS), disruption of biofilm formation, compromise of cell membrane integrity, enzyme inhibition, and protein denaturation [48]. The larger zone of inhibition against *S. aureus* observed in this study, compared to the studies referenced, supports this finding. This can be explained by the fact that the composition and properties of the essential oil may vary depending on factors such as the country of harvest, altitude, duration of sunlight exposure, and harvesting conditions.

4 Conclusion

As a result, undoped and Dysprosium (Dy^{3+}), Terbium (Tb^{3+}) doped Tin Oxide (SnO_2) NPs were synthesized using a green synthesis-supported co-precipitation approach and subsequently characterized employing X-ray Diffraction (XRD), Thermogravimetric Analysis (TGA), Scanning Electron Microscopy (SEM), Energy Dispersive Spectroscopy (EDS), and Photoluminescence (PL) measurements. The XRD and EDS analyses substantiated the successful integration of Dy^{3+} and Tb^{3+} elements within the SnO_2 host matrix. TGA analyses, wherein only a weight loss of 1–3% was recorded within the 30–600 °C temperature interval, validated the elevated thermal stability of the synthesized samples. The PL spectra for both Dy^{3+}/Tb^{3+}-doped samples exhibited distinct sharp peaks that corresponded to the transitions from excited states to ground states of Dy^{3+} and Tb^{3+} ions. It was noted that the PL intensities associated with the transitions of the Dy^{3+}/Tb^{3+} ion in co-doped SnO_2 markedly increased in comparison to those of the singly doped samples. This observation indicates a more efficient energy transfer mechanism occurring from Dy^{3+} to Tb^{3+}. The temperature-dependent behavior of the emission characteristics of co-doped SnO2 was further investigated. From the color coordinates, it was determined that the emission color of the doped SnO_2 samples resides within the white spectral region at room temperature, while shifting toward the yellowish-green region at cryogenic temperatures (10 K), suggesting promising color tuning potential for low-temperature optoelectronic applications. The findings of this study clearly demonstrate the color tunability of the synthesized samples and show that they exhibit promising color tuning potential suitable for yellowish-green light-emitting diodes (LEDs) at cryogenic temperatures. Additionally, NPs containing SnO_2 and Laurus nobilis L. extract exhibited effective levels of antibacterial activity against E. coli and S. aureus at all concentrations; however, the antibacterial activity of these compounds was observed to be more effective against S. aureus than against E. coli.

Acknowledgements The authors thank to the Research Funds of Balikesir University (Grant No. BAP-2024/037) for the financial support and Balikesir University, Science and Technology Application and Research Center (BUBTAM) for the use of the Photoluminescence Spectrometer. Additionally, we would also like to thank Fuatcan Hadanoglu for his invaluable assistance in sourcing the initial chemical materials.

Author Contributions Mustafa Burak Coban: Writing - original draft, Supervision, Software, Writing–original draft, Writing–review & editing, Conceptualization, Visualization & Methodology. Ozgen Omur Pekel: Conceptualization, Methodology and Visualization. Remziye Tulek: Conceptualization, Methodology. Ali Teke: Visualization & Methodology. Guler Yagiz Erdemir: Software. Orkun Babacan: Conceptualization and Visualization. Fatma Unal: Conceptualization, Methodology and Visualization. Berna Kocer Kizilduman: Visualization & Methodology. Mehmet Dogan: Software & Visualization.

Funding Open access funding provided by the Scientific and Technological Research Council of Türkiye (TÜBİTAK).

Data Availability Data will be made available on request.

Declarations

Competing interests The authors declare that they have no known competing financial interests or personal relationships that could have appeared to influence the work reported in this paper.

Open Access This article is licensed under a Creative Commons Attribution 4.0 International License, which permits use, sharing, adaptation, distribution and reproduction in any medium or format, as long as you give appropriate credit to the original author(s) and the source, provide a link to the Creative Commons licence, and indicate if changes were made. The images or other third party material in this article are included in the article's Creative Commons licence, unless indicated otherwise in a credit line to the material. If material is not included in the article's Creative Commons licence and your intended use is not permitted by statutory regulation or exceeds the permitted use, you will need to obtain permission directly from the copyright holder. To view a copy of this licence, visit http://creativecommons.org/licenses/by/4.0/.

References

1. Elamin NY, Indumathi T, Ranjith Kumar E (2023) Evaluation of physicochemical and biological properties of SnO_2 and Fe doped SnO_2 nanoparticles. Ceram Int 49:2388–2393. https://doi.org/10.1016/j.ceramint.2022.09.211
2. Arif M, Shah MZU, Ahmad SA, Shah MS, Ali Z, Ullah A et al (2022) High photocatalytic performance of copper-doped SnO_2 nanoparticles in degradation of Rhodamine B dye. Opt Mater 134:113135. https://doi.org/10.1016/j.optmat.2022.113135

3. Kaur H, Bhatti HS, Singh K (2023) Tb-doped SnO_2 nanostructures for fluorescence sensing and dye degradation applications. J Mater Sci Mater Electron 34:1428. https://doi.org/10.1007/s10854-023-10843-7
4. Wang L, Ma S, Xu X, Li J, Yang T, Cao P et al (2021) Oxygen vacancy-based Tb-doped SnO_2 nanotubes as an ultra-sensitive sensor for ethanol detection. Sens Actuators B Chem 344:130111. https://doi.org/10.1016/j.snb.2021.130111
5. Batzill M, Diebold U (2005) The surface and materials science of tin oxide. Prog Surf Sci 79:47–154. https://doi.org/10.1016/j.progsurf.2005.09.002
6. Singha KK, Srivastava SK (2025) Influence of Sb/Ag doping on dielectric, resistivity, current–voltage and magnetic characteristics of SnO_2 compounds. Next Materials 8:100692. https://doi.org/10.1016/j.nxmate.2025.100692
7. Hoang Huy VP, Nguyen TMH, Bark CW (2023) Recent advances of doped SnO2 as electron transport layer for high-performance Perovskite solar cells. Materials 16:6170. https://doi.org/10.3390/ma16186170
8. Pinto AH, Nogueira AE, Dalmaschio CJ, Frigini IN, de Almeida JC, Ferrer MM et al (2022) Doped tin dioxide (d-SnO_2) and its nanostructures: review of the theoretical aspects, photocatalytic and biomedical applications. Solids 3:327–360. https://doi.org/10.3390/solids3020024
9. Amutha T, Rameshbabu M, Sasi Florence S, Senthilkumar N, Vetha Potheher I, Prabha K (2019) Studies on structural and optical properties of pure and transition metals (Ni, Fe and co-doped Ni–Fe) doped tin oxide (SnO_2) nanoparticles for anti-microbial activity. Res Chem Intermed 45:1929–1941. https://doi.org/10.1007/s11164-018-03713-z
10. Chen C, Li Y, Shen M (2020) Structure-related luminescent properties induced by doping in Sm-doped SnO_2 hollow spheres. Ceram Int 46:17025–17033. https://doi.org/10.1016/j.ceramint.2020.03.289
11. Cojocaru B, Avram D, Kessler V, Parvulescu V, Seisenbaeva G, Tiseanu C (2017) Nanoscale insights into doping behavior, particle size and surface effects in trivalent metal doped SnO_2. Sci Rep 7:9598. https://doi.org/10.1038/s41598-017-09026-2
12. Feng P, Zhang J, Qin Q, Hu R, Wang Y (2014) Hydrothermal synthesis and afterglow luminescence properties of hollow SnO_2:Sm^{3+},Zr^{4+} spheres for potential application in drug delivery. Mater Res Bull 50:365–368. https://doi.org/10.1016/j.materresbull.2013.11.011
13. Pillai SK, Sikhwivhilu LM, Hillie TK (2010) Synthesis, characterization and photoluminescence properties of Dy^{3+}-doped nanocrystalline SnO2. Mater Chem Phys 120:619–624. https://doi.org/10.1016/j.matchemphys.2009.12.010
14. Unal F (2022) The effects of precursor concentration and morphology on photoluminescence behavior of Tb_2O_3 phosphors. J Chin Chem Soc 69:332–338. https://doi.org/10.1002/jccs.202100480
15. Villagrán Z, Anaya-Esparza LM, Velázquez-Carriles CA, Silva-Jara JM, Ruvalcaba-Gómez JM, Aurora-Vigo EF et al (2024) Plant-based extracts as reducing, capping, and stabilizing agents for the green synthesis of inorganic nanoparticles. Resources 13:70. https://doi.org/10.3390/resources13060070
16. Singh H, Desimone MF, Pandya S, Jasani S, George N, Adnan M et al (2023) Revisiting the green synthesis of nanoparticles: uncovering influences of plant extracts as reducing agents for enhanced synthesis efficiency and its biomedical applications. Int J Nanomedicine 18:4727–4750. https://doi.org/10.2147/IJN.S419369
17. Pradeep M, Kruszka D, Kachlicki P, Mondal D, Franklin G (2022) Uncovering the Phytochemical Basis and the Mechanism of Plant Extract-Mediated Eco-Friendly Synthesis of Silver Nanoparticles Using Ultra-Performance Liquid Chromatography Coupled with a Photodiode Array and High-Resolution Mass Spectrometry. ACS Sustain Chem Eng 10:562–571. https://doi.org/10.1021/acssuschemeng.1c06960
18. Nations U The Sustainable Development Goals Report 2025. https://unstats.un.org/sdgs/report/2025
19. Al-Azawi AH (2022) Evaluation of Antibacterial Activity of Laurus nobilis Leaves Extract against Escherichia. coli Isolates 21:623–631
20. El Malti J, Amarouch H (2009) Antibacterial, effect histological impact and oxidative stress studies from *Laurus nobilis* extract. J Food Qual 32:190–208. https://doi.org/10.1111/j.1745-4557.2009.00245.x
21. Ibrahim RN (2021) Study Antibact Activity Laurus Nobilis Leaves 54:18–24
22. Sancer O, Şahin U, Çetin ES, Tepebaşi MY, Cezaroğlu Y, Bilir G et al (2024) Effect of *Laurus nobilis* on bacteria and human transforming growth factor-β1. Rev Assoc Med Bras. https://doi.org/10.1590/1806-9282.20230683
23. Quinn PJ, Markey BK, Leonard FC, FitzPatrick ES, Fanning S, Hartigan PJ (2011) Veterinary Microbiology and icrobial Disease 2nd Edition. vol. 2
24. Bauer AW, Kirby WM, Sherris JCTM, Bauer A, Kirby W, Sherris J, Turck M (1966) Susceptibility testing by a standardized single disc method. Am J Clin Pathol 45
25. Shkir M, AlAbdulaal TH, Manthrammel MA, Khan FS (2024) Novel MgO and Ag/MgO nanoparticles green-synthesis for antibacterial and photocatalytic applications: a kinetics-mechanism & recyclability. J Photochem Photobiol A Chem. https://doi.org/10.1016/j.jphotochem.2023.115398
26. Coban MB (2018) Hydrothermal synthesis, crystal structure, luminescent and magnetic properties of a new mononuclear Gd^{III} coordination complex. J Mol Struct 1162:109–116. https://doi.org/10.1016/j.molstruc.2018.02.089
27. Hakami J, Kaynar UH, Coban MB, Aydin H, Alamri R, Jabali DA et al (2025) Optical performance and luminescence properties of Dy^{3+}-doped $LaMgB_5O_{10}$ phosphors. Inorg Chem Commun 171:113540. https://doi.org/10.1016/j.inoche.2024.113540
28. Alsam AA, Kaynar UH, Aydin H, Coban MB, Canimoglu A, Can N (2025) Enhanced luminescence and quenching mechanisms in Na^+ co-doped $K_7CaY_2(B_5O_{10})_3$:Tb^{3+} phosphors under UV radiation. Appl Radiat Isot 217:111635. https://doi.org/10.1016/j.apradiso.2024.111635
29. Souadi G, Madkhli AY, Kaynar UH, Gok C, Aydin H, Coban MB et al (2025) Photoluminescence properties and structural analysis of Tb^{3+}-doped $K_3Gd(BO_2)_6$: a first study on negative thermal quenching. J Alloys Compd 1010:178147. https://doi.org/10.1016/j.jallcom.2024.178147
30. Altowyan AS, Kaynar UH, Aydin H, Hakami J, Coban MB, Cikrikci K et al (2025) Synthesis, structural characterization, and photoluminescence properties of Dy^{3+}-doped CaB_4O_7 phosphors: influence of Li^+ and K^+ co-doping. Mater Sci Semicond Process 195:109593. https://doi.org/10.1016/j.mssp.2025.109593
31. Coban MB (2019) Magnetic and photophysical properties of new TbIII –based two-dimensional hydrogen-bonded polymer. J Mol Struct 1177:331–337. https://doi.org/10.1016/j.molstruc.2018.09.077
32. Sharma G, Singh K, Manupriya, Mohan S, Singh H, Bindra S (2006) Effects of gamma irradiation on optical and structural properties of $PbO–Bi_2O_3–B_2O_3$ glasses. Radiat Phys Chem 75:959–966. https://doi.org/10.1016/j.radphyschem.2006.02.008
33. Holliday K (1999) Inorganic Condensed Matter, Applications of Luminescence Spectroscopy. Encycl Spectrosc Spectrom 933–943. https://doi.org/10.1006/rwsp.2000.0132
34. den Engelsen D, Fern GR, Ireland TG, Harris PG, Hobson PR, Lipman A et al (2016) Ultraviolet and blue cathodoluminescence from cubic Y_2O_3 and Y_2O_3:Eu^{3+} generated in a transmission electron microscope. J Mater Chem C 4:7026–7034. https://doi.org/10.1039/C6TC01750A

35. Coban MB, Diken ME, Dogan S, Kara Subasat H, Structural (2023) Thermal, Optical and Antibacterial Properties of Co-doped (Dy^{3+}/Eu^{3+}):PEG+PVA Novel Transparent Hybrid Films. J Inorg Organomet Polym Mater 33:2924–2942. https://doi.org/10.1007/s10904-023-02724-7
36. Kaczkan M, Malinowski M, Suchocki A, Pawlak DA, Turczyński S (2020) Temperature and concentration dependent luminescence of Yb^{3+} centers in YAM. J Alloys Compd 842:155893. https://doi.org/10.1016/j.jallcom.2020.155893
37. Lv Q, Shao B, Ma X, Yang S, Wang C, Dong Y et al (2023) A novel efficient red-emitting $K_7SrY_2B_{15}O_{30}$: Eu^{3+} phosphor with non-concentration quenching and robust thermal stability for white LEDs. Spectrochim Acta A Mol Biomol Spectrosc 287:122126. https://doi.org/10.1016/j.saa.2022.122126
38. Gu M, Jin X, Huang S, Liu X, Liu B, Ni C (2010) The effects of GeO_2 adulterant on the luminescence properties of Tb-doped silicate glasses. Opt Mater 32:1022–1027. https://doi.org/10.1016/j.optmat.2010.02.024
39. Souadi G, Amri N, Kaynar ÜH, Coban MB, Madkhali O, Ayvacikli M et al (2024) Novel Sm^{3+} doped $YCa_4O(BO_3)_3$ phosphors: structural and, low and room temperature luminescent insights. Appl Radiat Isot 203:111114. https://doi.org/10.1016/j.apradiso.2023.111114
40. Kavas KN, Gungor E, Acar Y, Unal F, Eroglu O, Diken ME et al (2025) Fabrication of novel Li^+ and Sm^{3+} doped CeO_2@PVP orangish-red luminescent hybrid nanofiber for investigation of structural, optical and antibacterial activity: unusual electronic transition modification by Li^+ doping. Ceram Int 51:49517–49533. https://doi.org/10.1016/j.ceramint.2025.08.192
41. Lakshminarayana G, Kaky KM, Baki SO, Lira A, Caldiño U, Kityk IV et al (2017) Optical absorption, luminescence, and energy transfer processes studies for Dy^{3+}/Tb^{3+}-codoped borate glasses for solid-state lighting applications. Opt Mater 72:380–391. https://doi.org/10.1016/j.optmat.2017.06.030
42. Ashrafi-Saiedlou S, Rasouli-Sadaghiani M, Fattahi M (2025) Green synthesis of iron oxide nanoparticles using *Thymus migricus* for multifunctional applications in antioxidant, antimicrobial, photocatalytic, and seed priming processes. Heliyon 11:e42933. https://doi.org/10.1016/j.heliyon.2025.e42933
43. Haq S, Rehman W, Waseem M, Shah A, Khan AR, Rehman MU et al (2020) Green synthesis and characterization of tin dioxide nanoparticles for photocatalytic and antimicrobial studies. Mater Res Express. https://doi.org/10.1088/2053-1591/ab6fa1
44. Mohammed HA, Eddine LS, Souhaila M, Hasan GG, Kir I, Abdullah JAA (2024) Green synthesis of SnO2 nanoparticles from *Laurus nobilis* L. extract for enhanced gelatin-based films and CEF@SnO2 for efficient antibacterial activity. Food Bioprocess Technol. https://doi.org/10.1007/s11947-023-03209-8
45. Gopal S, Iruson B, Balaraman S, Krishnmoorthy S, Elayaperumal M (2023) Effect on Optical and Antibacterial Activity of SnO_2 and CuO Blended SnO_2 Nanoparticles. Soft Nanosci Lett 13:1–12. https://doi.org/10.4236/snl.2023.132001
46. Pandimurugan AR, Sankaranarayanan K (2022) Antibacterial and photocatalytic activity of ZnO, SnO_2 and Zn_2SnO_4 nanoparticles prepared by Microwave assisted method. Mater Technol. https://doi.org/10.1080/10667857.2021.1873635
47. John N, Somaraj M, Tharayil NJ (2018) Synthesis, Characterization and Anti - Bacterial Activities of SnO2 Nanoparticles Using Biological Molecule. IOP Conf. Ser Mater Sci Eng 360. https://doi.org/10.1088/1757-899X/360/1/012007
48. Siriken B, Yavuz C, Guler A (2018) Antibacterial Activity of Laurus nobilis: A review of literature. Med Sci Discov. https://doi.org/10.17546/msd.482929

Publisher's Note Springer Nature remains neutral with regard to jurisdictional claims in published maps and institutional affiliations.